INTERNATIONAL JOURNAL FOR NUMERICAL METHODS IN FLUIDS
Int. J. Numer. Meth. Fluids 2009; **59**:593–609
Published online 9 July 2008 in Wiley InterScience (www.interscience.wiley.com). DOI: 10.1002/fld.1833

Numerical simulation of liquid crystalline polymer flow into two-dimensional thin cavity moulds

Jianye Sun*, †

Harbin University of Science and Technology, No. 52, Xuefu Road, Nangang District, Harbin 150080, People's Republic of China

SUMMARY

In this paper, flows of liquid crystalline polymers into two-dimensional thin cavity moulds are simulated. The flows are modelled by Ericksen–Leslie equations of motion in the high viscosity limit. An elliptic pressure equation is derived under Hele–Shaw approximations, and the non-isothermal natures of the flow are modelled. The equations are solved using the finite-difference technique. A new boundary-mapping technique is developed in this study to solve the difficulty in the finite-difference treatment of arbitrarily shaped boundaries, which possess no natural coordinate system. This new method avoids the difficult mesh control in the body-fitted mapping process and makes the mapping process easy to implement. It can also solve the problems caused by the uneven distribution of grid nodes in the traditional body-fitted mapping technique. Copyright © 2008 John Wiley & Sons, Ltd.

Received 13 August 2007; Revised 22 March 2008; Accepted 30 March 2008

KEY WORDS: partial differential equations; finite-difference methods; boundary-fitted mapping; liquid crystal polymer flow; Navier–Stokes; non-Newtonian

1. INTRODUCTION

Liquid crystalline polymers (LCPs) have a high degree of long-range molecular orientational order, thereby being referred to as anisotropic fluids. When such LCPs are processed, the resulting solid polymer maintains the high molecular orientational order of LCPs and consequently exhibits special properties in comparison with traditional polymers. Therefore, it is very valuable to predict the development of the molecular orientations during the processing of the LCPs.

At present, Leslie–Ericksen (L–E) theory and Doi's theory are the two popular constitutive theories for liquid crystals. The L–E theory, which is based on macroscopic continuum mechanics, is suitable for describing the rheological properties of low molecular weight nematics. Doi's theory,

*Correspondence to: Jianye Sun, Room 201, Unit 4, A Building, 'Jiao-Gong-Zhi-Jia', No. 14, Zhongxing Street, Nangang District, Harbin 150080, Heilongjiang Province, People's Republic of China.
†E-mail: jnysun@yahoo.com

derived from microscopic molecular theory, is a kinetic model for rod-like polymers. Usually Doi's model is too complicated to be used in the simulation of complex flows. As mentioned by Chang *et al.* [1], Kuzuu and Doi have demonstrated that Doi's theory could be reduced to the L–E theory in the limit of low shear rates. Many researchers, such as Chono and Tsuji [2], Chang *et al.* [1], Güler [3], Baleo *et al.* [4] and Vanderheyden and Ryskin [5] have used the L–E theory in analysing the flow-induced behaviour of LCPs.

This paper presents a numerical method to predict the transient director orientations of nematic LCPs in Hele–Shaw flows. The Ericksen–Leslie equations of motion in the high viscosity limit were used to model the flows. From the momentum equation and the continuity equation, we derived an elliptic pressure equation that was solved by finite-difference method.

In this study, a new boundary-mapping technique was developed to solve the difficulty in the finite-difference treatment of arbitrarily shaped boundaries, which possess no natural coordinate system. Unlike the popular body-fitted mapping technique, which numerically maps the irregular shape of the flow field to a more regular shape in a computational domain where the governing equations are solved using the well-developed finite-difference schemes, the new technique only constructs a general curvilinear coordinate system for the boundaries of the flow domain. For the region inside boundaries, the governing equations are solved on the physical domain directly. This technique avoids the difficult mesh control in the body-fitted mapping process and makes the mapping process easy to implement. It can also solve the problems caused by the uneven distribution of grid nodes in the traditional body-fitted mapping technique.

2. MATHEMATICAL MODELLING

2.1. Hele–Shaw approximations

This study focuses on the LCP flows during injection moulding in thin-walled moulds, as shown in Figure 1. These flow fields can be approximated as Hele–Shaw flows in which one dimension (z-direction) is much smaller in comparison with the other two. As demonstrated by Altan *et al.* [6], this physical feature allows for the following simplifications: (1) viscous forces are dominant, and inertial forces can be neglected in the momentum equations; (2) flow and dynamic forces in the gapwise direction can be neglected; (3) shear stresses through the gap width are dominant and the in-plane stresses can be neglected, which means that the shear rates through the gap width are dominant and the in-plane shear rates can be neglected; and (4) the fluid is assumed incompressible.

2.2. Fluid motion

An elliptic pressure equation for isothermal nematics flows of fixed directors has been derived by Chono and Tsuji in [2]. In this study, the non-isothermal nematics flows of free directors are considered. As pointed out by Vanderheyden and Ryskin [5], LCPs exhibit very high viscosities and it is reasonable to use the high viscosity approximation in LCPs flows. The Ericksen–Leslie equations of motion in the high viscosity limit are given by

Continuity equation:

$$\nabla \cdot \mathbf{v} = 0 \tag{1}$$

DOI: 10.1002/fld

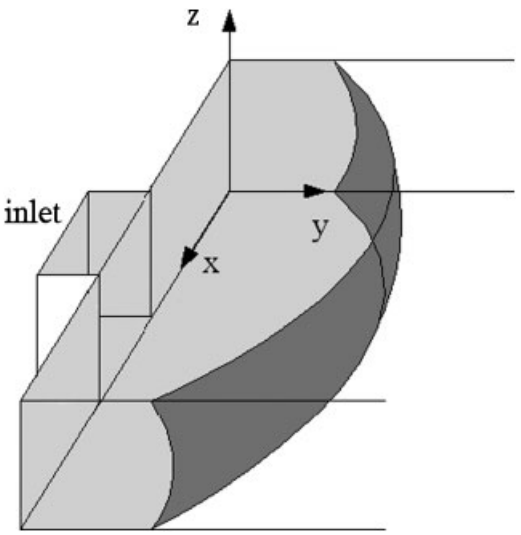

Figure 1. A Hele–Shaw-type flow in a mould cavity.

Momentum equation:

$$-\nabla p+\nabla\cdot\boldsymbol{\tau}=\mathbf{0} \tag{2}$$

Angular momentum equation:

$$\frac{\mathrm{D}\mathbf{n}}{\mathrm{D}t}=\mathbf{W}\cdot\mathbf{n}+\lambda(\mathbf{A}\cdot\mathbf{n}-\mathbf{n}\cdot\mathbf{A}\cdot\mathbf{nn}) \tag{3}$$

The stress tensor is given by

$$\boldsymbol{\tau}=\beta_0\mathbf{A}+\beta_1\mathbf{n}\cdot\mathbf{A}\cdot\mathbf{nnn}+\beta_2(\mathbf{nn}\cdot\mathbf{A}+\mathbf{A}\cdot\mathbf{nn}) \tag{4}$$

where $\mathbf{v}$ is the velocity vector, p is the pressure, λ is the tumbling parameter, β_0, β_1, and β_2 are constant viscosities, $\mathbf{n}$ is the director orientation vector, $\boldsymbol{\tau}$ is the stress tensor, $\mathbf{A}$ is the rate of strain tensor:

$$\mathbf{A}=\frac{(\nabla\mathbf{v})^{\mathrm{T}}+\nabla\mathbf{v}}{2} \tag{5}$$

and $\mathbf{W}$ is the vorticity tensor:

$$\mathbf{W}=\frac{\nabla\mathbf{v}-(\nabla\mathbf{v})^{\mathrm{T}}}{2} \tag{6}$$

According to Hele–Shaw approximations, the momentum equation (2) can be simplified as in the x-direction:

$$\frac{\partial p(x,y)}{\partial x}=\frac{\partial \tau_{zx}(x,y,z)}{\partial z} \tag{7a}$$

DOI: 10.1002/fld

in the y-direction:

$$\frac{\partial p(x,y)}{\partial y}=\frac{\partial \tau_{zy}(x,y,z)}{\partial z} \tag{7b}$$

The stress tensor equation (4) can be expressed as

$$\tau_{zx}=f_1(x,y,z)\frac{\partial v_x}{\partial z}+f_2(x,y,z)\frac{\partial v_y}{\partial z} \tag{8a}$$

$$\tau_{zy}=f_2(x,y,z)\frac{\partial v_x}{\partial z}+f_3(x,y,z)\frac{\partial v_y}{\partial z} \tag{8b}$$

where

$$f_1(x,y,z)=\frac{\beta_0}{2}+\beta_1\cdot n_x^2n_z^2+\frac{\beta_2}{2}(n_x^2+n_z^2)$$

$$f_2(x,y,z)=n_xn_y\left(\beta_1\cdot n_z^2+\frac{\beta_2}{2}\right)$$

$$f_3(x,y,z)=\frac{\beta_0}{2}+\beta_1\cdot n_y^2n_z^2+\frac{\beta_2}{2}(n_y^2+n_z^2)$$

Now consider an arbitrary point in the x–y plane. At this point, x and y are constants, and for an arbitrary function $f(x,y,z)$,

$$\frac{\partial f(x,y,z)}{\partial z}=\frac{\mathrm{d}f(x,y,z)}{\mathrm{d}z} \tag{9}$$

Integrating Equations (7a)–(7b) on z, we have

$$\tau_{zx}(x,y,z)=\frac{\partial p(x,y)}{\partial x}z+C_1(x,y) \tag{10a}$$

$$\tau_{zy}(x,y,z)=\frac{\partial p(x,y)}{\partial y}z+C_2(x,y) \tag{10b}$$

From Equations (8a)–(8b), we have

$$\frac{\partial v_x}{\partial z}=\frac{f_3}{f_1\cdot f_3-(f_2)^2}\tau_{zx}-\frac{f_2}{f_1\cdot f_3-(f_2)^2}\tau_{zy} \tag{11a}$$

$$\frac{\partial v_y}{\partial z}=\frac{f_1}{f_1\cdot f_3-(f_2)^2}\tau_{zy}-\frac{f_2}{f_1\cdot f_3-(f_2)^2}\tau_{zx} \tag{11b}$$

Substituting Equations (10a)–(10b) into Equations (11a)–(11b) and integrating on z, we have

$$v_x=\frac{\partial p}{\partial x}\int_0^z\frac{f_3}{D}z'\,\mathrm{d}z'-\frac{\partial p}{\partial y}\int_0^z\frac{f_2}{D}z'\,\mathrm{d}z'+C_1\int_0^z\frac{f_3}{D}\,\mathrm{d}z'-C_2\int_0^z\frac{f_2}{D}\,\mathrm{d}z' \tag{12a}$$

$$v_y=-\frac{\partial p}{\partial x}\int_0^z\frac{f_2}{D}z'\,\mathrm{d}z'+\frac{\partial p}{\partial y}\int_0^z\frac{f_1}{D}z'\,\mathrm{d}z'-C_1\int_0^z\frac{f_2}{D}\,\mathrm{d}z'+C_2\int_0^z\frac{f_1}{D}\,\mathrm{d}z' \tag{12b}$$

DOI: 10.1002/fld

where

$$D = f_1 \cdot f_3 - (f_2)^2$$

Considering $v_x(x, y, h) = 0$ and $v_y(x, y, h) = 0$, we have

$$C_1 = E_1 \frac{\partial p}{\partial x} + E_2 \frac{\partial p}{\partial y}$$

$$C_2 = E_3 \frac{\partial p}{\partial x} + E_4 \frac{\partial p}{\partial y}$$

$$E_1 = \frac{R_{20}R_{21} - R_{10}R_{31}}{R_{10}R_{30} - R_{20}^2}$$

$$E_2 = \frac{R_{10}R_{21} - R_{20}R_{11}}{R_{10}R_{30} - R_{20}^2}$$

$$E_3 = \frac{R_{30}R_{21} - R_{20}R_{31}}{R_{10}R_{30} - R_{20}^2}$$

$$E_4 = \frac{R_{20}R_{21} - R_{11}R_{30}}{R_{10}R_{30} - R_{20}^2}$$

$$R_{ij} = \int_0^h \frac{f_i z^j}{D} \, \mathrm{d}z$$

where h is the gap width.

The approximate continuity equation of Hele–Shaw flows can be expressed as

$$\frac{\partial(h\overline{v}_x)}{\partial x} + \frac{\partial(h\overline{v}_y)}{\partial y} = 0 \tag{13}$$

where $\overline{v}_x$ and $\overline{v}_y$ represent the averages of velocities v_x and v_y on the gap width.

The interval $[0, h]$ is divided into N small intervals of equal widths, Δ. For a bounded integrable function $f(z)$,

$$\int_0^h \int_0^z f \, \mathrm{d}z' \, \mathrm{d}z = \lim_{N\to\infty} \sum_{i=1}^{N} \sum_{j=1}^{i} f_j \Delta^2 = \lim_{N\to\infty} \sum_{j=1}^{N} f_j \cdot (N - j + 1)\Delta^2 = \int_0^h f \cdot (h - z) \, \mathrm{d}z \tag{14}$$

where f_j represents the value of function f at the left point of the jth small interval.

Substituting Equations (12a)–(12b) into Equation (13), and using Equation (14), we have

$$G_1 \frac{\partial^2 p}{\partial x^2} + (G_1 + G_2) \frac{\partial^2 p}{\partial x \partial y} + G_2 \frac{\partial^2 p}{\partial y^2} + \left(\frac{\partial G_1}{\partial x} + \frac{\partial G_3}{\partial y} \right) \frac{\partial p}{\partial x} + \left(\frac{\partial G_2}{\partial x} + \frac{\partial G_4}{\partial y} \right) \frac{\partial p}{\partial y} = 0 \tag{15}$$

DOI: 10.1002/fld

where

$$G_1 = S_{31} + E_1 S_{30} - E_3 S_{20}$$

$$G_2 = -S_{21} + E_2 S_{30} - E_4 S_{20}$$

$$G_3 = -S_{21} - E_1 S_{20} + E_3 S_{10}$$

$$G_4 = S_{11} - E_2 S_{20} + E_4 S_{10}$$

$$S_{ij} = \int_0^h \frac{f_i z^j}{D}(h-z)\,\mathrm{d}z$$

Equation (15) is the final elliptic pressure equation.

2.3. Viscosities

The six Leslie viscosities are given by Larson [7] as

$$\alpha_1 = -2\eta R^2(p) S_4 \tag{16a}$$

$$\alpha_2 = -\eta R(p)\left(1+\frac{1}{\lambda}\right) S_2 \tag{16b}$$

$$\alpha_3 = -\eta R(p)\left(1-\frac{1}{\lambda}\right) S_2 \tag{16c}$$

$$\alpha_4 = \eta R^2(p)\tfrac{2}{35}(7-5S_2-2S_4)+\alpha_0 \tag{16d}$$

$$\alpha_5 = \eta R(p)[\tfrac{1}{7}R(p)(3S_2+4S_4)+S_2] \tag{16e}$$

$$\alpha_6 = \eta R(p)[\tfrac{1}{7}R(p)(3S_2+4S_4)-S_2] \tag{16f}$$

where η is the characteristic viscosity, S_2 and S_4 are the second and fourth moments of the molecule distribution function, and $R(p)$ is a parameter that depends on the effective aspect ratio p of the rigid molecules and is given as

$$R(p) = \frac{p^2-1}{p^2+1} \tag{17}$$

The term α_0 is expected to be negligible for polymeric nematics [7].

The second and fourth moments S_2 and S_4, whose Maier–Saupe values are shown in Table I, are given by Larson [7]. The other values of S_2 and S_4 are obtained by interpolation. Here T represents the liquid crystal polymer temperature, and T_{NI} represents the transforming temperature from the nematic state into the isotropic state.

The tumbling parameter λ can be obtained by the following simple approximation form [7]:

$$\lambda = R(p)\frac{5S_2+16S_4+14}{35S_2} \tag{18}$$

DOI: 10.1002/fld

Table I. S_2 and S_4 from the Maier–Saupe theory.

T/T_{NI}	S_2	S_4
0.999	0.441	0.127
0.990	0.471	0.145
0.985	0.485	0.154
0.975	0.509	0.171
0.965	0.530	0.186
0.955	0.549	0.200
0.945	0.566	0.213
0.930	0.588	0.232
0.920	0.602	0.244
0.910	0.615	0.256
0.900	0.627	0.268
0.880	0.649	0.290
0.860	0.669	0.311
0.840	0.687	0.331
0.800	0.719	0.370
0.715	0.772	0.446
0.505	0.864	0.619
0.303	0.926	0.775

The characteristic viscosity η can be obtained from fits to the viscosity data of the liquid at temperature above T_{NI}, at which the liquid is in the isotropic state and has no orientational order, so that $S_2 = S_4 = 0$. Then the Newtonian viscosity η_{iso} of this isotropic liquid is given by [7]

$$\eta_{iso} = \frac{\alpha_4}{2} = \frac{\eta}{5} \tag{19}$$

Shenoy and Saint measured the viscosity of liquid crystalline melts of copolymers of ethylene terephthalate (ETP) and *p*-hydroxy benzoic acid (HBA) in a range of shear rates and temperatures and at different polymer compositions. Their data for the 60 mol% HBA: 40 mol% ETP composition have been fitted by Lekakou [8]. The result of Lekakou, which is shown in the following equation, was used as η_{iso} in this study:

$$\eta_{iso} = 8.18 \times 10^{-4} \dot{\gamma}^{0.82-1} e^{6752/T} \tag{20}$$

where T is the absolute temperature of the liquid crystalline melts.

The coefficients used in the governing equations are given by

$$\beta_0 = \alpha_4 \tag{21a}$$

$$\beta_1 = \alpha_1 - \lambda(\alpha_2 + \alpha_3) \tag{21b}$$

$$\beta_2 = \alpha_5 + \lambda\alpha_2 \tag{21c}$$

2.4. Heat transfer

The energy equation for incompressible LCPs can be expressed as

$$\rho C_v \frac{DT}{Dt} = (\nabla \cdot \mathbf{q}) + (\boldsymbol{\tau} : \nabla \mathbf{v}) \tag{22}$$

DOI: 10.1002/fld

where ρ is the density, C_v is the heat capacity per unit mass, $\mathbf{q}$ is the heat flow, T is the temperature, and $\boldsymbol{\tau}$ is the stress tensor.

The heat flow $\mathbf{q}$ for LCPs is given by

$$\mathbf{q}=\beta_{t1}(\mathbf{n}\cdot\nabla T)\mathbf{n}+\beta_{t2}\nabla T \tag{23}$$

where β_{t1} and β_{t2} are the thermal conductivity coefficients with β_{t1} expressing the anisotropy.

In the Hele–Shaw flow, we can assume that heat conduction in the gapwise direction is dominant and in-plane heat conduction can be neglected. The energy equation can be simplified as

$$\rho C_v\frac{\mathrm{D}T}{\mathrm{D}t}=\alpha\frac{\partial^2 T}{\partial z^2}+\beta\frac{\partial T}{\partial z}+(\boldsymbol{\tau}:\nabla\mathbf{v}) \tag{24}$$

where

$$\alpha=\beta_{t1}n_z^2+\beta_{t2}$$

$$\beta=\beta_{t1}n_z\left(\frac{\partial n_x}{\partial x}+\frac{\partial n_y}{\partial y}+2\frac{\partial n_z}{\partial z}\right)+\beta_{t1}\left(n_x\frac{\partial n_z}{\partial x}+n_y\frac{\partial n_z}{\partial y}\right)$$

3. SOLUTION METHODS

3.1. Grid generation

The finite-difference treatment of arbitrarily shaped boundaries, which possesses no natural coordinate system, proves to be more difficult. In general, a body-fitted curvilinear mesh can be generated over any irregular body by essentially mapping the boundaries of the irregular shape from the physical domain to a more regular, prescribed shape in a computational domain. An orthogonal, rectangular mesh can be created on the transformed, simpler domain and then mapped back to provide a curvilinear mesh on the original irregular shape. The governing equations similarly can be transformed and solved on the computational domain, using the well-established finite-difference techniques, and the solutions at every node are mapped back onto the physical domain.

Usually Poisson-type elliptic expressions are used to relate the physical (x, y) coordinates to the computational (ξ, η) coordinates due to their inherent 'smoothness' and the ability to handle boundary discontinuities. These relations are

$$\frac{\partial^2\xi}{\partial x^2}+\frac{\partial^2\xi}{\partial y^2}=P(\xi,\eta) \tag{25a}$$

$$\frac{\partial^2\eta}{\partial x^2}+\frac{\partial^2\eta}{\partial y^2}=Q(\xi,\eta) \tag{25b}$$

In the above equations, P and Q are grid control functions that can be used to specify mesh concentration in desired areas.

This scheme has been successfully used in the finite-difference solution of the equations for flows inside irregularly shaped two-dimensional bodies by many researchers. However, the selection of P and Q is not an easy task. Most researchers set them equal to zero. This simplification works well

DOI: 10.1002/fld

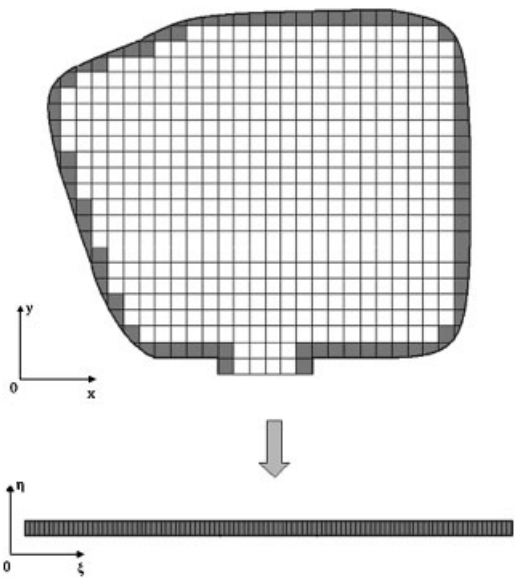

Figure 2. The numerical mapping of the boundary of an irregular flow domain (from the physical x, y coordinates) to a more regular computational domain (in the ξ, η coordinates).

for some situations, but the selection of P and Q is still necessary for flow domains of complicated shapes. To solve this problem, we developed the so-called 'boundary-mapping' technique. As shown in Figure 2, only the boundary of the flow domain takes part in the mapping process. Obviously the mesh concentration control is not necessary and P and Q can be set equal to zero for arbitrarily shaped flow domains. At the grid points on the boundary, the governing equations are transformed and solved on the computational domain, and the solutions at every boundary node were mapped back onto the physical domain. At the grid points inside boundaries, the governing equations are solved on the physical domain directly. The mapping equations of the new method and the traditional method are same. Therefore, the two methods should be of the same level accuracy.

This new boundary-mapping technique avoids the difficult mesh control in the body-fitted mapping process and makes the mapping process easy to implement. The grid nodes generated by the new method are evenly distributed. Therefore, it could solve the problems caused by the uneven distribution of grid nodes in the traditional body-fitted mapping technique.

3.2. Transformation of the governing equations

$$\frac{\partial p}{\partial x} = \frac{\partial p}{\partial \xi}\frac{\partial \xi}{\partial x} + \frac{\partial p}{\partial \eta}\frac{\partial \eta}{\partial x} \tag{26a}$$

$$\frac{\partial p}{\partial y} = \frac{\partial p}{\partial \xi}\frac{\partial \xi}{\partial y} + \frac{\partial p}{\partial \eta}\frac{\partial \eta}{\partial y} \tag{26b}$$

$$\frac{\partial^2 p}{\partial x^2} = \frac{\partial^2 p}{\partial \xi^2}\left(\frac{\partial \xi}{\partial x}\right)^2 + 2\frac{\partial^2 p}{\partial \xi \partial \eta}\frac{\partial \xi}{\partial x}\frac{\partial \eta}{\partial x} + \frac{\partial^2 p}{\partial \eta^2}\left(\frac{\partial \eta}{\partial x}\right)^2 \tag{26c}$$

DOI: 10.1002/fld

$$\frac{\partial^2 p}{\partial y^2} = \frac{\partial^2 p}{\partial \xi^2}\left(\frac{\partial \xi}{\partial y}\right)^2 + 2\frac{\partial^2 p}{\partial \xi \partial \eta}\frac{\partial \xi}{\partial y}\frac{\partial \eta}{\partial y} + \frac{\partial^2 p}{\partial \eta^2}\left(\frac{\partial \eta}{\partial y}\right)^2 \tag{26d}$$

$$\frac{\partial^2 p}{\partial x \partial y} = \frac{\partial^2 p}{\partial \xi^2}\frac{\partial \xi}{\partial x}\frac{\partial \xi}{\partial y} + \frac{\partial^2 p}{\partial \xi \partial \eta}\frac{\partial \xi}{\partial y}\frac{\partial \eta}{\partial x} + \frac{\partial^2 p}{\partial \xi \partial \eta}\frac{\partial \xi}{\partial x}\frac{\partial \eta}{\partial y} + \frac{\partial^2 p}{\partial \eta^2}\frac{\partial \eta}{\partial x}\frac{\partial \eta}{\partial y} \tag{26e}$$

Substituting Equations (26a)–(26e) into Equations (15), we have

$$a_1\frac{\partial^2 p}{\partial \xi^2} + a_2\frac{\partial^2 p}{\partial \xi \partial \eta} + a_3\frac{\partial^2 p}{\partial \eta^2} + a_4\frac{\partial p}{\partial \xi} + a_5\frac{\partial p}{\partial \eta} = 0 \tag{27}$$

where

$$a_1 = G_1\left(\frac{\partial \xi}{\partial x}\right)^2 + (G_2+G_3)\frac{\partial \xi}{\partial x}\frac{\partial \xi}{\partial y} + G_4\left(\frac{\partial \xi}{\partial y}\right)^2$$

$$a_2 = 2G_1\frac{\partial \xi}{\partial x}\frac{\partial \eta}{\partial x} + (G_2+G_3)\left(\frac{\partial \xi}{\partial x}\frac{\partial \eta}{\partial y} + \frac{\partial \xi}{\partial y}\frac{\partial \eta}{\partial x}\right) + 2G_4\frac{\partial \xi}{\partial y}\frac{\partial \eta}{\partial y}$$

$$a_3 = G_1\left(\frac{\partial \eta}{\partial x}\right)^2 + (G_2+G_3)\frac{\partial \eta}{\partial x}\frac{\partial \eta}{\partial y} + G_4\left(\frac{\partial \eta}{\partial y}\right)^2$$

$$a_4 = \left(\frac{\partial G_1}{\partial x} + \frac{\partial G_3}{\partial y}\right)\frac{\partial \xi}{\partial x} + \left(\frac{\partial G_2}{\partial x} + \frac{\partial G_4}{\partial y}\right)\frac{\partial \xi}{\partial y}$$

$$a_5 = \left(\frac{\partial G_1}{\partial x} + \frac{\partial G_3}{\partial y}\right)\frac{\partial \eta}{\partial x} + \left(\frac{\partial G_2}{\partial x} + \frac{\partial G_4}{\partial y}\right)\frac{\partial \eta}{\partial y}$$

Equation (27) is the pressure equation in the transformed domain.
From Equations (12a)–(12b), we have

$$h\overline{v}_x = G_1\frac{\partial p}{\partial x} + G_2\frac{\partial p}{\partial y} \tag{28a}$$

$$h\overline{v}_y = G_3\frac{\partial p}{\partial x} + G_4\frac{\partial p}{\partial y} \tag{28b}$$

Then,

$$h\overline{v}_\xi = h\overline{v}_x\frac{\partial \xi}{\partial x} + h\overline{v}_y\frac{\partial \xi}{\partial y} \tag{29a}$$

$$h\overline{v}_\eta = h\overline{v}_x\frac{\partial \eta}{\partial x} + h\overline{v}_y\frac{\partial \eta}{\partial y} \tag{29b}$$

DOI: 10.1002/fld

Substituting Equations (28a)–(28b) into Equations (29a)–(29b), we have

$$h\overline{v}_\xi = r_1\frac{\partial p}{\partial \xi} + r_2\frac{\partial p}{\partial \eta} \tag{30a}$$

$$h\overline{v}_\eta = r_3\frac{\partial p}{\partial \xi} + r_4\frac{\partial p}{\partial \eta} \tag{30b}$$

where

$$r_1 = \frac{\partial \xi}{\partial x}\left(G_1\frac{\partial \xi}{\partial x} + G_3\frac{\partial \xi}{\partial y}\right) + \frac{\partial \xi}{\partial y}\left(G_2\frac{\partial \xi}{\partial x} + G_4\frac{\partial \xi}{\partial y}\right)$$

$$r_2 = \frac{\partial \eta}{\partial x}\left(G_1\frac{\partial \xi}{\partial x} + G_3\frac{\partial \xi}{\partial y}\right) + \frac{\partial \eta}{\partial y}\left(G_2\frac{\partial \xi}{\partial x} + G_4\frac{\partial \xi}{\partial y}\right)$$

$$r_3 = \frac{\partial \xi}{\partial x}\left(G_1\frac{\partial \eta}{\partial x} + G_3\frac{\partial \eta}{\partial y}\right) + \frac{\partial \xi}{\partial y}\left(G_2\frac{\partial \eta}{\partial x} + G_4\frac{\partial \eta}{\partial y}\right)$$

$$r_4 = \frac{\partial \eta}{\partial x}\left(G_1\frac{\partial \eta}{\partial x} + G_3\frac{\partial \eta}{\partial y}\right) + \frac{\partial \eta}{\partial y}\left(G_2\frac{\partial \eta}{\partial x} + G_4\frac{\partial \eta}{\partial y}\right)$$

4. SIMULATION RESULTS AND DISCUSSION

In this section, the simulation results of the injection moulding of LCPs with a constant inlet pressure are presented. The shape of the mould cavity is approximately 7 cm wide, 10 cm long, and has a gap width of 3 mm. The melt was considered to enter the cavity at an inlet temperature of 300°C. A constant inlet pressure of 60 atm was assumed during the filling stage. The simulation is programmed in FORTRAN and run on a DELL notebook computer. The common iteration algorithm was used in the solution of Equations (15) and (27).

4.1. Using the traditional mapping technique

Mapping relations:

$$\frac{\partial^2 \xi}{\partial x^2} + \frac{\partial^2 \xi}{\partial y^2} = 0 \tag{31a}$$

$$\frac{\partial^2 \eta}{\partial x^2} + \frac{\partial^2 \eta}{\partial y^2} = 0 \tag{31b}$$

The body-fitted curvilinear meshes generated under Equations (31a)–(31b) are demonstrated in Figure 3. In this simulation a mesh of 101 nodes by 101 nodes was used.

The mould temperature is assumed to be 250°C. Figure 4(a) shows the locations of the free surfaces at various times during the filling operations. The filling time is approximately 7.2 s.

DOI: 10.1002/fld

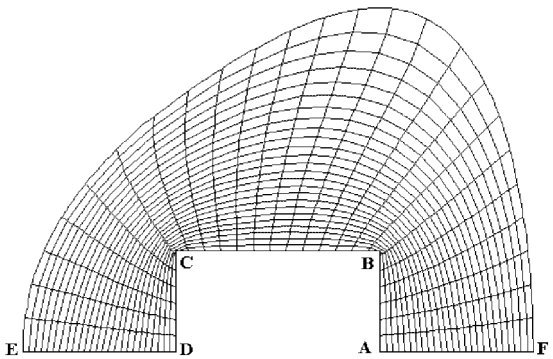

Figure 3. The body-fitted curvilinear mesh.

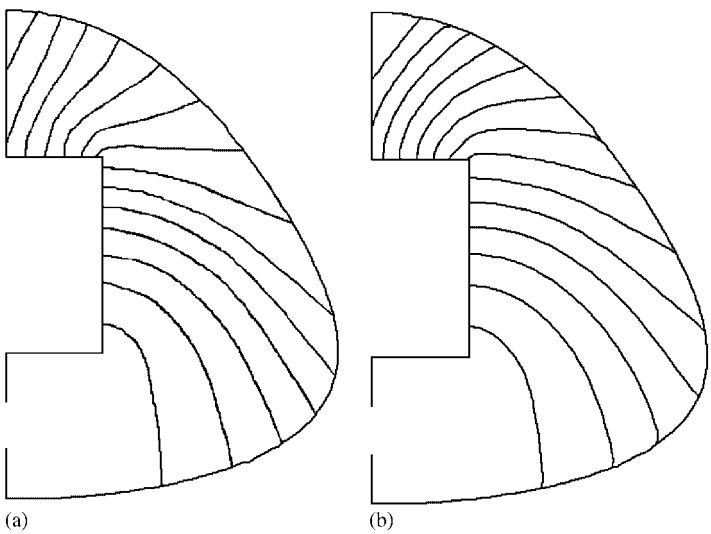

Figure 4. The free surface locations at various time, time interval = 0.5 s, mould temperature = 250°C: (a) traditional mapping technique and (b) new mapping technique.

As shown in Figure 3, the grid intervals along $ABCD$ are smaller than those along EF. Therefore, the computation accuracies of pressures and velocities along EF are lower. These differences in computation accuracies and their accumulation during the filling process may cause distortions of the flow fronts, as shown in Figure 4(a). This is a disadvantage of the traditional mapping technique. This problem may be solved by the new 'boundary-mapping' technology. In addition, due to the uneven distribution of grid nodes, more grid nodes are necessary to guarantee the computation accuracy in the whole flow domain. This causes more computation cost. In this study, it took approximately 15 h in computation when using the traditional mapping technique, which is in contrast to the approximately 2 h when using the new boundary-mapping technique.

DOI: 10.1002/fld

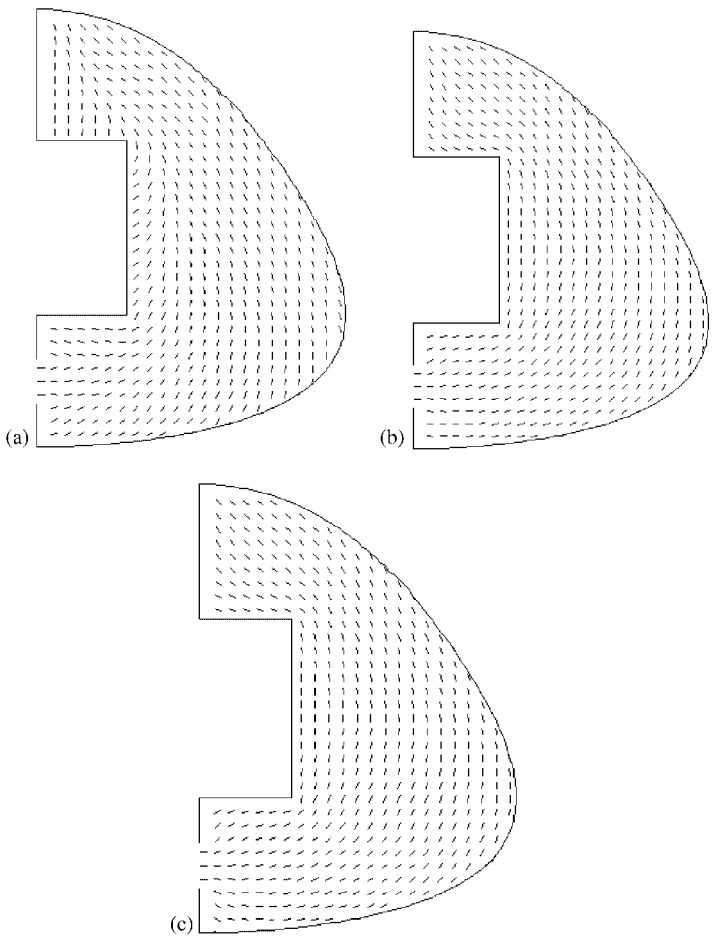

Figure 5. Director orientations at different layers, mould temperature = 250°C: (a) $z = 0.5$ gap size (centre); (b) $z = 0.25$ gap size; and (c) $z = 0.1$ gap size.

4.2. Using the new boundary-mapping technique

The mould temperature is assumed to be 250°C. Figure 4(b) shows the locations of the free surface at various times during the filling operations. The filling time is approximately 7.4 s. The simulation results near the completion of the filling stage are shown in Figures 5 and 6. Figure 5 shows the director orientation distributions in the x–y plane for three different heights in the mould gap width. The temperature distributions are displayed in Figure 6.

The simulation results when the mould temperature is equal to 200°C are shown in Figures 7–9.

It can be seen that the director orientations align the flowing directions near the mould wall when the mould temperature is 250°C and are irregular near the mould wall when the mould temperature is 200°C.

Except in the central core, Hele–Shaw flows can be treated as a simple shear flow. Therefore, the director orientations show the phenomenon of aligning when tumbling parameter λ is larger

DOI: 10.1002/fld

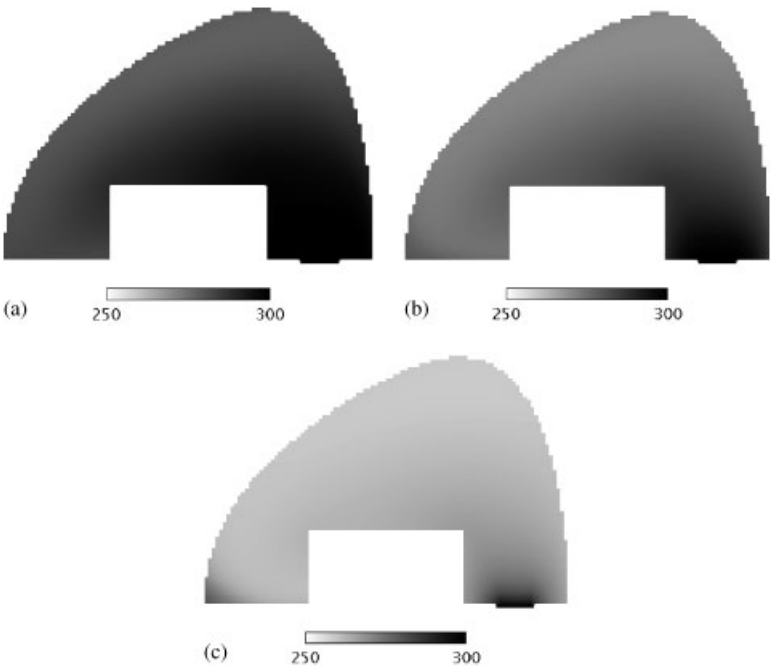

Figure 6. Temperature distributions at different layers, mould temperature = 250°C: (a) $z = 0.5$ gap size (centre); (b) $z = 0.25$ gap size; and (c) $z = 0.1$ gap size.

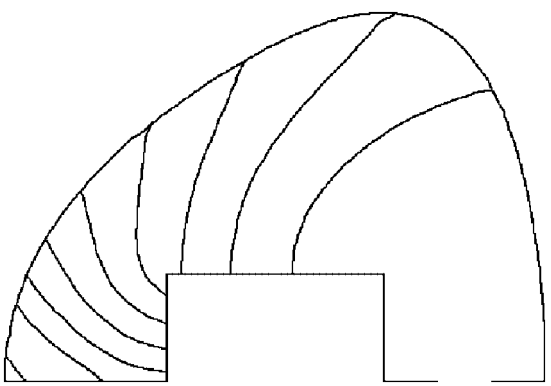

Figure 7. The free surface locations at various time, time interval = 1.5 s, mould temperature = 200°C.

than 1 and tumbling when λ is less than 1. According to Table I and Equation (18), λ is a function of temperature. As shown in Figure 10, when the temperature is more than $0.927T_{NI}$, λ is larger than 1; when temperature is lower than $0.927T_{NI}$, λ is larger than 1. When $T_{NI} = 300$°C, $0.927T_{NI} \approx 258.2$°C. Therefore, when the mould temperature is 250°C, the flow near the wall is

DOI: 10.1002/fld

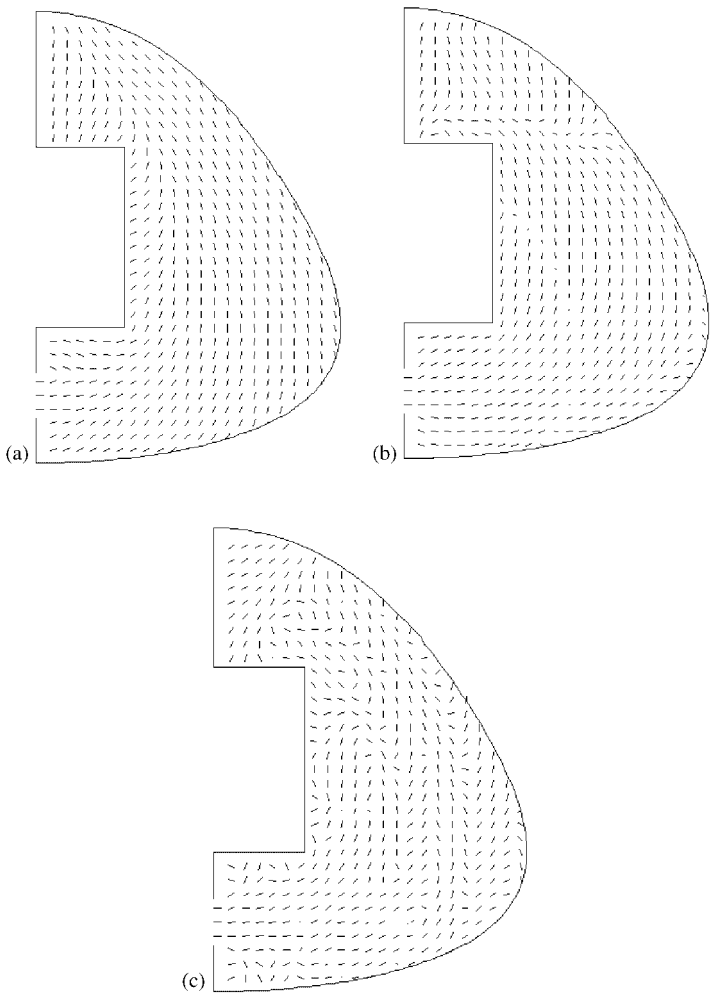

Figure 8. Director orientations at different layers, mould temperature = 200°C: (a) $z = 0.5$ gap size (centre); (b) $z = 0.25$ gap size; and (c) $z = 0.1$ gap size.

aligning, as shown in Figure 5(c); the phenomenon of tumbling appears as the mould temperature equals 200°C, as shown in Figure 8(b) and (c).

5. CONCLUSION

In this paper, a numeric simulation approach of injection moulding process of LCPs is presented. The corresponding technique can predict the locations of melt front at selected time steps during the injection and the director orientation distributions at various time steps. The LCP flows are modelled by Ericksen–Leslie equations of motion in the high viscosity limit. An elliptic pressure

DOI: 10.1002/fld

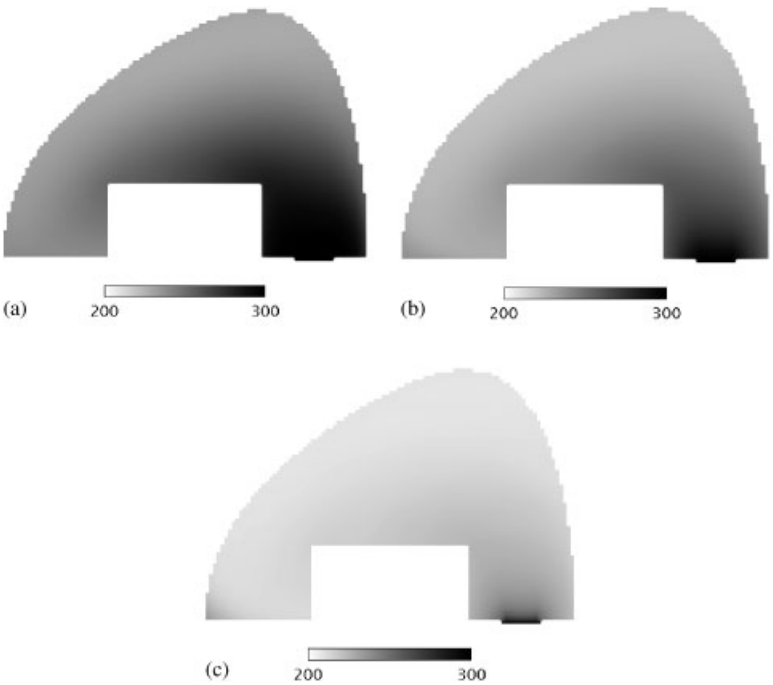

Figure 9. Temperature distributions at different layers, mould temperature = 200°C: (a) $z = 0.5$ gap size (centre); (b) $z = 0.25$ gap size; and (c) $z = 0.1$ gap size.

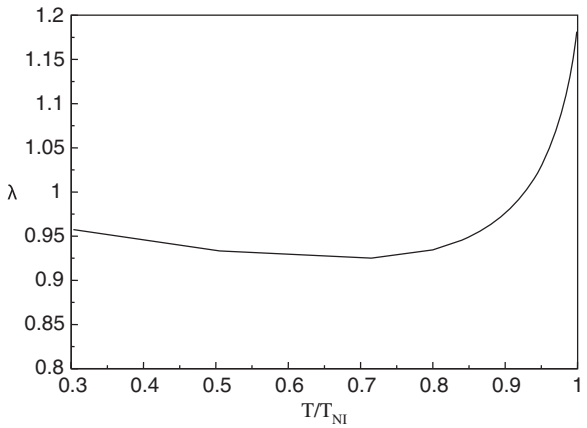

Figure 10. The relation between tumbling parameters λ and T/T_{NI}.

equation was derived under Hele–Shaw approximations, which was solved by finite-difference method. A new 'boundary-mapping' technique was developed to solve the difficulty in the finite-difference treatment of arbitrarily shaped boundaries. It may solve the problems caused by the

DOI: 10.1002/fld

uneven distribution of grid nodes in the traditional body-fitted mapping technique. It can also avoid the difficult mesh control in the body-fitted mapping process and reduce the computation time to some extent.

REFERENCES

1. Chang R-Y, Shiao F-C, Yang W-L. Simulation of director orientation of liquid crystalline polymers in 2-D flows. *Journal of Non-Newtonian Fluid Mechanics* 1994; **55**:1–20.
2. Chono S, Tsuji T. Computer simulation of flow and defect of nematic liquid crystal. *EKISHO* 1999; **3**(2):107–116 (in Japanese).
3. Güler M. Symbolic evaluation of the Ericksen–Leslie equations in the computation domain. *Journal of Non-Newtonian Fluid Mechanics* 1994; **52**:309–321.
4. Baleo JN, Vincent M, Navard P. Finite-element simulation of flow and director orientation of viscous anisotropic fluids in complex 2D geometries. *Journal of Rheology* 1992; **36**(4):663–701.
5. Vanderheyden WB, Ryskin G. Computer simulation of flow and molecular orientation in liquid crystal polymers. *Journal of Non-Newtonian Fluid Mechanics* 1987; **23**:383–414.
6. Cengiz Altan M, Subbiah S, Gucerl SI, Byron Pipes R. Numerical prediction of three-dimensional fiber orientation in Hele–Shaw flows. *Polymer Engineering and Science* 1990; **30**(14):848–859.
7. Larson RG. *The Structure and Rheology of Complex Fluids*. Oxford University Press: Oxford, 1999; 455–459.
8. Lekakou C. Mathematical modeling and computer simulations of the flow, nematic phase orientation, and heat transfer in thermotropic liquid crystalline polymers. *Polymer Engineering and Science* 1997; **37**(3):529–540.

DOI: 10.1002/fld